AIP | Physics of Fluids

Effects of magnetic fields on magnetohydrodynamic cylindrical and spherical Richtmyer-Meshkov instability

W. Mostert, V. Wheatley, R. Samtaney, and D. I. Pullin

Citation: Physics of Fluids **27**, 104102 (2015); doi: 10.1063/1.4932110
View online: http://dx.doi.org/10.1063/1.4932110
View Table of Contents: http://scitation.aip.org/content/aip/journal/pof2/27/10?ver=pdfcov
Published by the AIP Publishing

PHYSICS OF FLUIDS **27**, 104102 (2015)

Effects of magnetic fields on magnetohydrodynamic cylindrical and spherical Richtmyer-Meshkov instability

W. Mostert,[1] V. Wheatley,[1] R. Samtaney,[2] and D. I. Pullin[3]
[1]*School of Mechanical and Mining Engineering, University of Queensland, Queensland 4072, Australia*
[2]*Mechanical Engineering, King Abdullah University of Science and Technology, Thuwal, Saudi Arabia*
[3]*Graduate Aeronautical Laboratories, 301-46, California Institute of Technology, Pasadena, California 91125, USA*

(Received 29 June 2015; accepted 17 September 2015; published online 6 October 2015)

The effects of seed magnetic fields on the Richtmyer-Meshkov instability driven by converging cylindrical and spherical implosions in ideal magnetohydrodynamics are investigated. Two different seed field configurations at various strengths are applied over a cylindrical or spherical density interface which has a single-dominant-mode perturbation. The shocks that excite the instability are generated with appropriate Riemann problems in a numerical formulation and the effect of the seed field on the growth rate and symmetry of the perturbations on the density interface is examined. We find reduced perturbation growth for both field configurations and all tested strengths. The extent of growth suppression increases with seed field strength but varies with the angle of the field to interface. The seed field configuration does not significantly affect extent of suppression of the instability, allowing it to be chosen to minimize its effect on implosion distortion. However, stronger seed fields are required in three dimensions to suppress the instability effectively. © *2015 AIP Publishing LLC.* [http://dx.doi.org/10.1063/1.4932110]

NOMENCLATURE

MHD	Magnetohydrodynamic(s)
RM	Richtmyer-Meshkov [instability]
ICF	Inertial confinement fusion
IFS	Incident fast shock
TF	Transmitted fast shock
RF	Reflected fast shock
IFS-DI	Fast shock interaction with the density interface
HD	Hydrodynamic(s)
RT	Rayleigh-Taylor [instability]
DI	Density interface
ISS	Incident slow shock
TS	Transmitted sub-fast wave
RS	Reflected sub-fast wave
ISS-DI	Slow shock interaction with the density interface

I. INTRODUCTION

Inertial confinement fusion (ICF)[1] is a promising candidate for the generation of fusion energy. In this approach, a small capsule filled with deuterium-tritium fuel mixture is illuminated by intense radiation which causes the shell material to rapidly ablate, in turn driving an imploding shock. If the process is successful, this compresses the fuel to temperatures and pressures sufficient to initiate a fusion burn. The fuel is constrained by the inertia of the imploding flow.

One factor which limits the operating parameters of ICF is the presence of hydrodynamic instabilities, in particular the Richtmyer-Meshkov (RM)[2,3] and Rayleigh-Taylor (RT)[4,5] instabilities, which serve to break the spherisymmetry of the flow, limiting the potential for energy production. The RM instability arises as the imploding shock wave processes the density interface(s) in the target, depositing baroclinically generated vorticity; the RT instability of those same interfaces appears due to the radial acceleration of the fluid downstream of the shock.[1] In this investigation, we focus primarily on the RM instability in imploding flows such as these.

As the imploding shock wave converges, the fuel is ionized to a high extent so that it may be modelled as a plasma. One framework which is sometimes used for modelling the dynamics of plasmas is magnetohydrodynamics (MHD), and recent research to suggest that the RM instability is suppressed in MHD in the presence of a seed magnetic field: Samtaney[6] first noted its suppression in a uniform seed magnetic field for a planar shock accelerating a density interface inclined to the magnetic field; Wheatley *et al.*[7–9] later examined the mechanism of the suppression and extended the literature to transverse-[10] and general oblique-field[11] planar flow cases, while Sano *et al.*[12] theoretically and numerically investigated the critical strength of a magnetic field required for suppression of the planar RM instability, finding it to depend on the Mach number of the incident shock.

Other recent research investigates the application of seed fields to implosions such as those seen in ICF: Hohenberger *et al.* and related studies[13,14] conducted experimental investigations with the OMEGA laser on neutron yield in ICF targets under axial magnetic fields, seeing improvement in neutron yield and citing electron confinement as a contributing mechanism for this improvement; and in a computational approach, using the LASNEX radiation-hydrodynamics code, Perkins *et al.*[15] noted an increased robustness of the ICF process with respect to outer perturbation amplitude in the presence of similar seed axial magnetic fields.

Seed fields in the area of fusion energy are also of interest in the emerging Magnetized Liner Inertial Fusion (MagLIF) concept, outlined, for example, by Sefkow *et al.*,[16] which involves an axial magnetic field applied to implosions driven by a Z-pinch (a comprehensive review of which is given by Haines[17]) with a view to improving stability of the implosion.

The choice of seed field configuration and strength has a clear effect on the dynamics and symmetry of MHD implosions. A recent computational study by Mostert *et al.*[18] investigated the dynamic features and symmetry properties of Riemann problems initialized within physically plausible field configurations, including uniform, saddle-point, and tangential configurations, and concluded that saddle-point configuration served to most effectively minimize asymmetry effects, while the tangential-field configuration exhibited potentially catastrophic symmetry-breaking features in three dimensions. (Here, asymmetry implies deviation from axi- or spherisymmetry depending on the case.)

In another study, Pullin *et al.*[19] conducted an analysis using Whitham's geometrical shock dynamics[20] paired with a numerical study on the behaviour of a MHD shock collapsing onto a line current of infinite extent, noting a peculiar tendency of the shock to weaken in terms of both pressure ratio and Mach number on collapse, contrary to the expected behaviour under equivalent conditions of a gas-dynamic shock (see, among others,[20] Chisnell[21]), a factor which may influence the ability of the collapsing flow to compress fuel to conditions conducive to ignition. These two studies thus in part highlighted potential drawbacks to injudicious use of a seed field to enhance implosions of this kind.

The RT instability in the presence of a seed field in MHD has been studied to some extent in planar flows,[22] and the behaviour of the hydrodynamic RM instability in converging geometries such as those in principle seen in ICF has been the subject of recent investigations.[23–25] Here we investigate the light-to-heavy (that is, the incident shock travels from the light fluid to the heavy) RM instability in the presence of seed fields in cylindrical and spherical implosions under two promising seed field configurations; these configurations are chosen from Mostert *et al.*[18] for their relative ability to minimize asymmetry in imploding MHD flows of this nature. We characterize the shock refraction processes, examine perturbation growth along the RM interface, and study the degree of asymmetry in interface geometry and perturbation growth. The applicability in principle of the given seed field configuration and strength on problems such as ICF is emphasized.

II. CYLINDRICAL RM INSTABILITY

The cylindrical problem is considered first. Sec. II A describes the formulation of the problem, including theoretical basis, construction of the density interface, Riemann problem initialization, and definition of the parameter space; Sec. II B describes the numerical method and convergence characteristics; and Sec. II C presents and discusses the resulting flows, including shock structure and the behaviour of the density interface.

A. Formulation

1. Equations of motion

We use the framework of ideal MHD, under the following non-dimensionalization, which will be maintained throughout this study:

$$\mathbf{x} = \frac{\hat{\mathbf{x}}}{L_0}, \quad t = \frac{\hat{t}}{L_0/\sqrt{\hat{p}_0/\hat{\rho}_0}}, \quad \rho = \frac{\hat{\rho}}{\hat{\rho}_0}, \quad p = \frac{\hat{p}}{\hat{p}_0}, \mathbf{u} = \frac{\hat{\mathbf{u}}}{\sqrt{\hat{p}_0/r\hat{h}o_0}}, \quad \mathbf{B} = \frac{\hat{\mathbf{B}}}{\sqrt{\mu_0\hat{p}_0}}, \tag{1}$$

with ρ the density, $\mathbf{v}$ the velocity, $\mathbf{B}$ the magnetic field, p the pressure, and μ_0 the permeability of free space. Carets signify dimensional variables. Other than in μ_0, the 0-subscript represents a reference value. Neglecting the effect of gravity, the non-dimensionalized equations of ideal MHD, as a continuous, single-fluid quasi-neutral plasma can then be written as[26]

$$\frac{\partial \rho}{\partial t} + \nabla \cdot (\rho \mathbf{v}) = 0, \tag{2}$$

$$\rho\left(\frac{\partial \mathbf{v}}{\partial t} + \mathbf{v} \cdot \nabla \mathbf{v}\right) + \nabla p - (\nabla \times \mathbf{B}) \times \mathbf{B} = 0, \tag{3}$$

$$\frac{\partial e}{\partial t} + \mathbf{v} \cdot \nabla e + (\gamma - 1) e \nabla \cdot \mathbf{v} = 0, \tag{4}$$

$$\frac{\partial \mathbf{B}}{\partial t} - \nabla \times (\mathbf{v} \times \mathbf{B}) = 0, \quad \nabla \cdot \mathbf{B} = 0, \tag{5}$$

where e is the specific internal energy given by

$$e = \frac{p}{(\gamma - 1)\rho}, \tag{6}$$

and γ is the plasma specific heat ratio, which is set, assuming a perfect gas, to $\gamma = 5/3$. Diffusive effects are neglected, assuming that they occur over a sufficiently larger time scale than advection effects.

2. Flow geometry and seed field configuration

The coordinate system is two-dimensional in both Cartesian (x, y) and polar (r, ϕ) forms, which are related by transformations $x = r\cos\phi$ and $y = r\sin\phi$. We investigate two-dimensional (cylindrical) implosions, whose initialized density fields can be seen in Figure 1. Two seed fields are applied. They are constructed as a uniform, unidirectional configuration and a non-uniform configuration with a saddle-point at the centre of the domain. We label each case with a prefix denoting geometry type, with C for cylindrical, and with a number denoting the field configuration with 1 for a uniform field and 3 for a saddle-point field, for consistency with the labelling system used by Mostert *et al.*[18] We will refer to a zero-field case with the number 0. The strength of each seed field is set according to a reference parameter β_{0I}, which is defined in terms of non-dimensionalized variables as

$$\beta_{0I} = 2\frac{p_0}{B_0^2}, \tag{7}$$

where B_0 is the field strength at a reference radius $r_0 = 1$ and $p_0 = 1$ is the reference pressure, set at the centre of the domain. The parameter β_{0I} is thus used as a global case parameter to describe

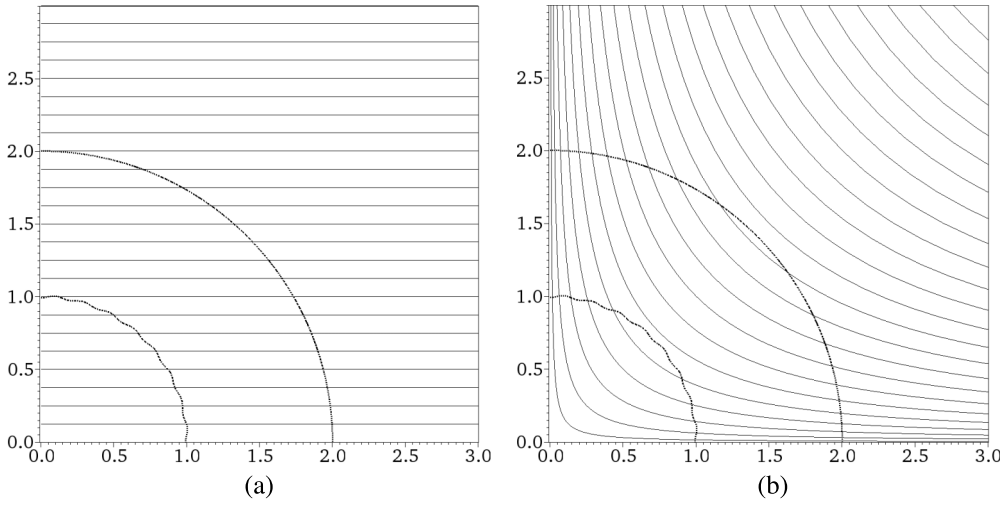

FIG. 1. Initial conditions showing perturbed density interface (inner) and Riemann interface (outer), with overlaid magnetic field lines for both cases. Shown with sinusoidal perturbation wavenumber $k = 32$. (a) Case C1. (b) Case C3.

the seed field magnetic pressure relative to the thermodynamic pressure. The subscript I indicates that the parameter is set according to the pressure inside the density interface (which we describe in Sec. II A 3), and the subscript 0 indicates that it is a reference quantity, as with most variables used in our framework. Following Mostert *et al.*, the field configurations are formulated as follows:

C1: Uniform, unidirectional field

$$\mathbf{B} = B_0 \hat{\mathbf{e}}_\mathbf{x}, \tag{8}$$

where $\hat{\mathbf{e}}_\mathbf{x}$ is the unit-vector corresponding to the x-direction.

C3: Saddle-point field

This field presents a saddle-point configuration. It can be generated by arranging four current arcs of infinite length, running in the z-direction (that is, out of plane) at specified locations (x_i, y_i), giving a field,[18]

$$\mathbf{B}(x,y) = \sum_{i=1}^{4} \left\{ \frac{\alpha_i B_0}{(x-x_i)^2 + (y-y_i)^2} \left[-(y-y_i)\hat{\mathbf{e}}_\mathbf{x} + (x-x_i)\hat{\mathbf{e}}_\mathbf{y} \right] \right\}, \tag{9}$$

with $\alpha_i = \{+\alpha_0, -\alpha_0, -\alpha_0, +\alpha_0\}$, a signed scaling parameter that sets $|\mathbf{B}(r_0)| = B_0$, and $(x_i, y_i) = \{(5,5), (-5,5), (-5,-5), (5,-5)\}$, chosen for convenience such that the current arcs lie sufficiently far outside the computational domain to avoid numerical issues with their singular magnetic fields.

In the work of Mostert *et al.*, an additional field configuration (C2, and the spherical analogue S2) was investigated; this field could be generated by passing a current in the z-direction through the Riemann interface (RI). While the field was cylindrical in both two- and three-dimensional geometries, in the latter case, it led to the formation of a high-pressure jet at the poles of the (spherical) Riemann interface that severely disrupted the spherisymmetry of the implosion, rendering the field configuration unfavourable with regard to minimizing implosion asymmetry.[18] For the field analysed by Pullin *et al.*, which could be generated by an axial line current of infinite extent in cylindrical geometry, the imploding MHD shock weakened to zero strength (in terms of pressure and Mach number) as it converged on the line current, adversely influencing its ability to compress fluid near the domain centre.[19] For these reasons, we do not consider these two fields here and limit our analysis to the C1 and C3 configurations described above.

3. Initial density interface

To provide an initial interface to be accelerated by the MHD shocks, whose initialization is to be described in Sec. II A 4, a perturbed density interface is constructed. This density interface is

TABLE I. Description of case abbreviations for cylindrical geometry, indicating field configuration, strength (with $\beta_{0I} = 2p_0/B_0^2$), and perturbation wavenumber k. These cases are run at unrefined mesh resolutions of 512^3 with three levels of refinement for effective resolutions of 2048^3. C0-cases have no seed field, C1-cases have uniform unidirectional seed field, and C3-cases have saddle-point field.

Case abbreviation	Field strength, β_{0I}	Wavenumber, k
C0-32	∞ (none)	32
C0-64	∞	64
C0-128	∞	128
C1-4-32	4	32
C1-4-64	4	64
C1-4-128	4	128
C1-32-32	32	32
C1-32-64	32	64
C1-32-128	32	128
C1-128-32	128	32
C1-128-64	128	64
C1-128-128	128	128
C3-4-32	4	32
C3-4-64	4	64
C3-4-128	4	128
C3-32-32	32	32
C3-32-64	32	64
C3-32-128	32	128
C3-128-32	128	32
C3-128-64	128	64
C3-128-128	128	128

characterized by an Atwood number

$$\mathcal{A} = \frac{\rho_0 - \rho_1}{\rho_0 + \rho_1} = 2/3, \tag{10}$$

where ρ_1 is the density of the fluid located outside the interface, which is the light fluid in the cases considered here. $\rho_0 = 1$ is the density of the fluid inside the interface and the reference density. The interface profile in density is given by the function,

$$\rho(r, \phi) = \frac{1}{2}\left(1 - \frac{|\mathcal{A}|}{\mathcal{A}} \tanh\left[\mu(r - \zeta_0(\phi))\right]\right), \tag{11}$$

which is a hyperbolic tangent function distributed around the reference radius $r_0 = 1$. This function regularizes the interface for purposes of smooth representation in a Cartesian computational mesh.

The density interface is perturbed with a single-mode sinusoid of azimuthal wavenumber k and with an amplitude equal to 4% of its wavelength. The perturbation function and initial amplitude are

$$\zeta_0(\phi) = r_0 - \eta_0 \cos k\phi, \qquad \eta_0 = \frac{2\pi}{25k}. \tag{12}$$

The hyperbolic tangent variation described in (11) does not then describe a strict discontinuity in density, but for convenience, we shall refer to it thus in this study.

Finally, for each field configuration, the field strength β_{0I} and perturbation wavenumber k are varied. Each case can be described according to an abbreviation outlined in Table I. These case abbreviations are used throughout the study.

4. Shock initialization

The cylindrical driving shock is initialized using a Riemann problem or RI consisting of two uniform initial states separated by the interface. The RI is initialized using regularization, without perturbation, as

$$\rho(r) = \frac{1}{2}\left(\rho_0 + \rho_b + (\rho_b - \rho_0)\tanh\left(\mu(r - r_b)\right)\right), \tag{13}$$

$$p(r) = \frac{1}{2}\left(p_0 + p_b + (p_b - p_0)\tanh\left(\mu(r - r_b)\right)\right), \tag{14}$$

where $\rho_b = 3\rho_0$ and $p_b = 12.1p_0$, allowing an initial approximate Mach number for the primary shocks at $\phi = 0$ of 2 for all cases. The RI is set at position $r_b = 2$. In the cylindrical geometry, the Mach number of the shock upon reaching the density interface (DI) at $r \simeq r_0$ is approximately 2.2 in the hydrodynamic (C0) cases. In the presence of a seed field (that is, C1 and C3 cases), the Mach number depends on the local fast magnetosonic speed and varies with field angle.

B. Methodology

1. Numerical method

For all cases, we use a numerical method developed by Samtaney,[27] which is a second-order nonlinear compressible finite volume code using an upwinding scheme with a Roe flux solver and projection method to enforce a divergence-free magnetic field; we also use a Cartesian adaptively refined mesh of the Berger-Colella type under the Chombo framework.[28] The criterion for grid refinement is $|\nabla\rho| > 0.02\rho$ on local ρ. Discretization is performed on a quarter-domain in the two-dimensional cases, and on an octant-domain in the three-dimensional cases, for $0 < x, y, z < l$ where $l = 3$.

The regularization parameter μ, which is the frequency argument of the hyperbolic tangent function, is determined by running one-dimensional Riemann problems with initial interfaces equivalent to the full problems, and chosen such that the initial Riemann interface width in cells is approximately equal to that of the fast MHD shock generated by the problem. For the two-dimensional simulations, $\mu = 1080$ to regularize the initial Riemann and density interface to approximately 5-6 cells along the Cartesian axes. This is a slightly conservative choice, since shocks of smaller thicknesses may appear in these simulations. The sensitivity of the Riemann problem itself to the choice of μ appears to be small, and we have assumed the same for the density interface evolution. A quantitative examination of the effect of μ on the dynamics of the whole Riemann problem and density interface evolution has not however been conducted in the present study.

2. Numerical convergence

The adaptively refined grid used in these simulations, described in Sec. II B 1, is tested for monotonic convergence using Richardson extrapolation, as described by Stern *et al.*[29] We consider the C1, strong field and high wavenumber case—that is, with $\beta_{0I} = 4$, $k = 128$—for base (unrefined) resolutions of 288^2, 384^2, and 512^2, with three levels of adaptive refinement to effective resolutions of 2304^2, 3072^2, and 4096^2. This corresponds to a refinement ratio between grids of $4/3$. We test this case because it features the strongest base magnetic field and the highest initial perturbation wavenumber, and thus is a suitable candidate for testing whether the behaviour of the perturbations is adequately resolved. The particular metric used in the Richardson extrapolation is the numerical integral of the graphs of amplitude η/η_0 over time, for the angular segment of the domain $0 < \phi < \pi/8$. This value is found to converge with an order $\simeq 2.3$ from the Richardson-extrapolated value. This value is greater than the formal order of the (second-order) numerical method in use, so it is limited to 2, with an associated estimated relative error of 1.2% on the finest mesh.

C. Results

The RM instability in these flows is characterized as follows. First, the shock refraction process is examined, including classification of the transmitted and reflected waves arising from the

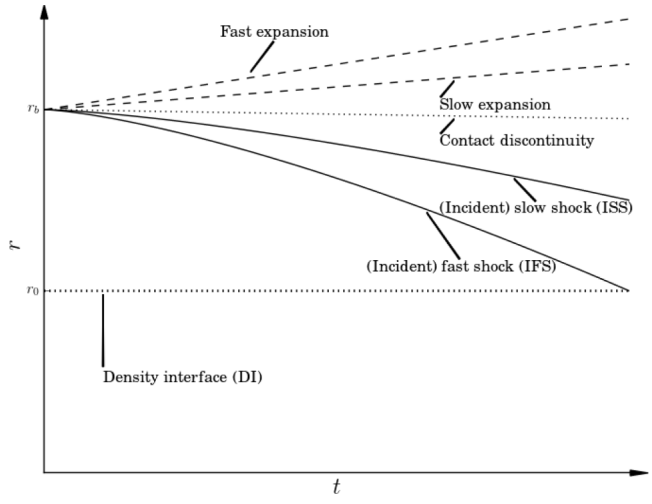

FIG. 2. Schematic radius-time diagram showing the Riemann problem along arbitrary ϕ prior to the shock-interface interaction. The slow and in particular the fast MHD shocks are the driver shocks in the converging RM problem. Density interface shown for reference, though not strictly part of the Riemann problem. At field orientation $\nu = 0$, no slow waves exist, and at $\nu = \pi/2$, the contact discontinuity becomes a MHD tangential discontinuity.

shock-interface interaction. Second, we present the growth of perturbations on the DI, highlighting any suppression that appears. Third, the effect of field configuration and strength on the symmetry of the DI as it implodes is considered.

The waves generated by the Riemann problem can be generally summarized as in the schematic, Figure 2. Our primary concern is the shock-interface interaction in the RM problem. Presently, interactions between the DI and the contact interface or the expansion systems resulting from the Riemann problem do not occur. There are therefore two expected shock interactions, in contrast to the single interaction (disregarding reshock) in gas-dynamic RM problems. We refer to the incoming fast MHD shock system as the *incident fast shock* (IFS) and the incoming slow MHD shock system as the *incident slow shock* (ISS).

The dynamics of the C3 Riemann problem qualitatively resemble an angularly compressed version of the C1 Riemann problem. That is, the dynamic features of the C1 Riemann problem, which vary over $\phi = [0, \pi/2]$ in that problem, appear in the C3 Riemann problem over an angular range of $\phi = [0, \pi/4]$. The $\phi = \pi/4$ ray in the C3 problem acts as a true line of symmetry in this geometry. Furthermore, a peculiar feature dubbed a "kink" appears at the field angle $\nu = \pi/2$ in the slow shock system; this field angle corresponds to a minimum in the slow characteristic speed and a discontinuity in the shock curvature. It is essentially a regular shock reflection, producing two additional reflected slow shocks downstream.[18]

Figure 3 shows density fields at a non-dimensional time of $t = 0.8$ from cylindrical low-wavenumber cases for zero-, uniform-, and saddle-field configurations with $\beta_{0I} = 4$ where appropriate. The perturbations under either field configurations are clearly much smaller than in the zero-field case, suggesting at a glance that the MHD RMI is suppressed. However, the perturbations, while remaining axisymmetric in C0, do not remain so in the C1 and C3 cases. The pattern of their suppression follows broadly the symmetry of the dynamics of the Riemann problem, with the perturbations appearing flat near $\nu \simeq \pi/2$ and at their largest near $\nu \simeq 0$. We therefore first characterize the shock refraction process that leads to this perturbation suppression in order to explain the asymmetric effect of the field configuration.

1. Wave structure

We consider first, as a reference problem, the uniform, unidirectional seed field case in cylindrical geometry under a strong field ($\beta_{0I} = 4$) and low perturbation wavenumber ($k = 32$). Using

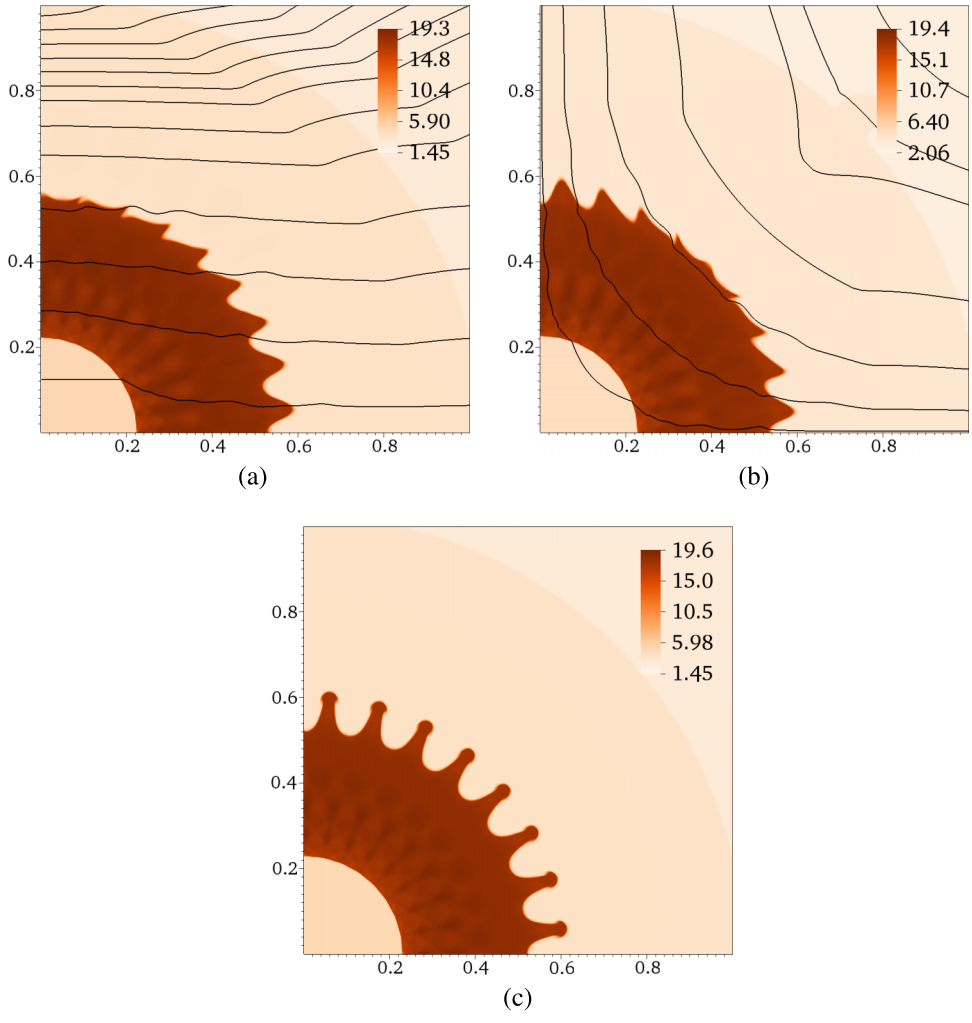

FIG. 3. Developed density fields low-wavenumber cylindrical cases at comparable time, $t = 0.8$. See Table I for descriptions of case abbreviations. (a) C1-32-32. (b) C3-32-32. (c) C0-32.

the abbreviations described in Table I, this is designated case C1-4-32. The two primary interactions are the interaction between the IFS and the DI (IFS-DI) and the ISS and the DI (ISS-DI). (See Nomenclature for descriptions of abbreviations.)

Figure 4 shows the developed flow visualizing vorticity for shocks with the DI indicated with a solid line and with overlaid magnetic field lines, after the IFS-DI interaction. In this interaction, a transmitted fast shock (TF), a transmitted sub-fast shock (TS), a reflected sub-fast shock (RS), and a reflected fast shock (RF) are produced.

Visualized in vorticity, Figure 4 exposes the suppression mechanism as follows. First, the IFS interacts with the DI, depositing baroclinic vorticity on it. Second, the DI, in regions everywhere except $\nu = \pi/2$, is a MHD contact discontinuity and therefore cannot carry vorticity, so this vorticity is carried away from it by the TS and RS waves. Third, at $\nu = \pi/2$, the vorticity remains close to the DI. Here, the TS and RS do not move away from the DI. The baroclinic vorticity around $\nu \simeq \pi/2$ is however still transported in directions parallel and antiparallel to the DI by TS and RS, leading to oscillation of the perturbation amplitudes in that region due to successive constructive and destructive interference between the waves. Generally speaking, then, across the domain, the vorticity-carrying TS and RS waves travel roughly along magnetic field lines. This mechanism is in line with the analyses of Samtaney and Wheatley *et al.* in planar flows.[6–8,10,11]

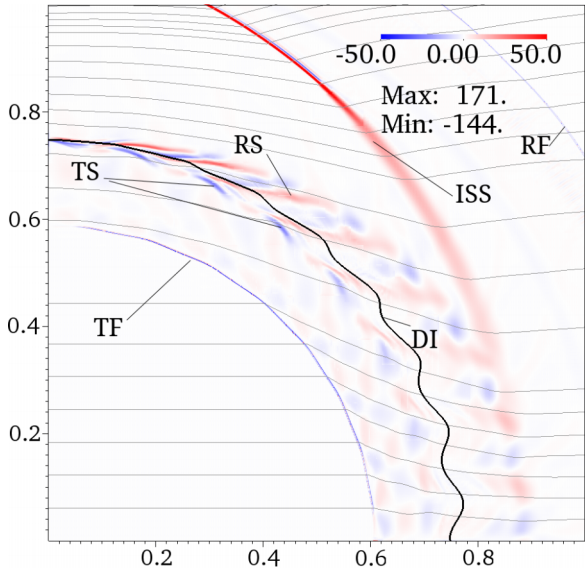

FIG. 4. Vorticity for case C1-4-32 at $t = 0.60$, with the DI shown with a solid line and overlaid magnetic field lines, showing transmitted and reflected waves resulting from IFS-DI interaction. See Table I for meaning of case abbreviation.

Figure 5 shows the flow during the ISS-DI interaction. This interaction is qualitatively different from the IFS-DI interaction. The ISS is non-axisymmetric and also weak in terms of pressure ratio near $\nu \simeq 0$, strengthening towards $\nu \simeq \pi/2$. Before processing the DI, the ISS first traverses the reflected waves RF and RS from the IFS-DI interaction. In traversing the RF wave, an additional, very weak, reflected slow shock is produced (not visible in Figure 5), but the trajectory of the ISS remains largely unchanged. However, in traversing the RS wave, the ISS is slowed and weakened further prior to reaching the DI, and the RS is refracted towards the ISS normal.

The ISS now passes through the DI very gradually, and owing to its low pressure ratio does not interact strongly with the DI. The largest pressure ratio across the shock system occurs at the

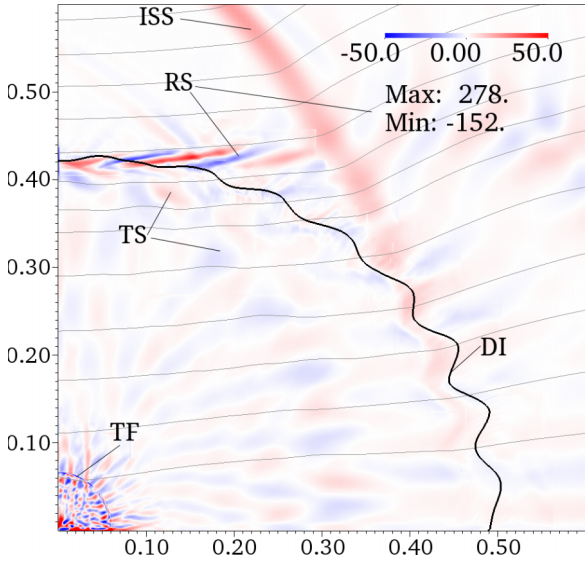

FIG. 5. Vorticity for C1-4-32 (see Table I) at $t = 0.91$, showing refraction of the ISS through the DI. Waves resulting from IFS-DI interaction labelled for context. The TF wave has reflected off the origin by this time and is travelling outward. Note the refraction of the RS wave toward the normal of the ISS.

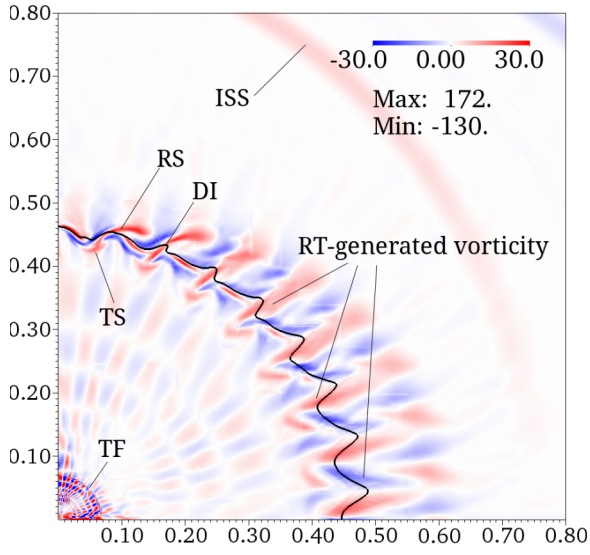

FIG. 6. Continuous baroclinic generation of vorticity at the DI due to RT-effects, case C1-32-32, at $t = 0.92$.

shock geometry kink at $\phi = \pi/2$ for the strong-field ($\beta_{0I} = 4$) case; for $k = 32$ at $t = 0.99$, this is approximately $\simeq 1.13$. By comparison, for the same case at $t = 0.35$, just prior to the IFS-DI interaction, the pressure ratio across the IFS at $\phi = \pi/2$ (its weakest point) is around $\simeq 4.7$.

In part because of the weakness of the ISS, any baroclinically generated vorticity or additional waves formed from the ISS-DI interaction are too weak to appear in these results. However, as the ISS penetrates the heavier fluid inside the DI it refracts toward the DI normal. Note that unlike the TF from the IFS, this "transmitted ISS" appears to maintain some degree of perturbation as it continues to move inwards past the DI.

Suppression of perturbation growth in the C3-cases follows the same mechanism as for C1-cases, with local field-line orientation roughly governing the direction of vorticity transport away from (or along) the DI. Mostert *et al.* note a lesser degree of asymmetry in C3 (and later, S3) cases in the dynamics of the imploding flow. This is reflected to some extent by the perturbations themselves—see Figure 3, comparing the general shape appearance of the perturbations between C1 and C3 at $t = 0.80$.

2. Rayleigh-Taylor effects

At later times, after the IFS-DI and before the ISS-DI interactions, there is additional vorticity that is generated at the DI, as shown in Figure 6. Unlike the vorticity previously generated during the IFS-DI interaction, this vorticity layer is generated continuously and also continuously advected away from the DI. The generation of this vorticity is a result of RT instability, which occurs due to the continuous acceleration of the DI as it moves radially inwards, manifesting through the baroclinic misalignment in pressure and density gradients that exists across the interface following the IFS-DI interaction. The advection of this vorticity away from the DI also suggests that the RT instability is suppressed in a manner similar to the RM instability, namely, by MHD waves which are generated continuously at the interface.

3. DI evolution

We now quantify the extent of the suppression of the RM instability and the variation of amplitude growth with the field angle ν. Figure 7 shows the full DI evolution for cases C0-32 and C1-32-32; the interface is plotted in (ϕ, r) space every $\Delta t = 0.1$, showing successive snapshots as the simulation progresses. The zero-field case (C0) shows the hydrodynamic RM instability. As the

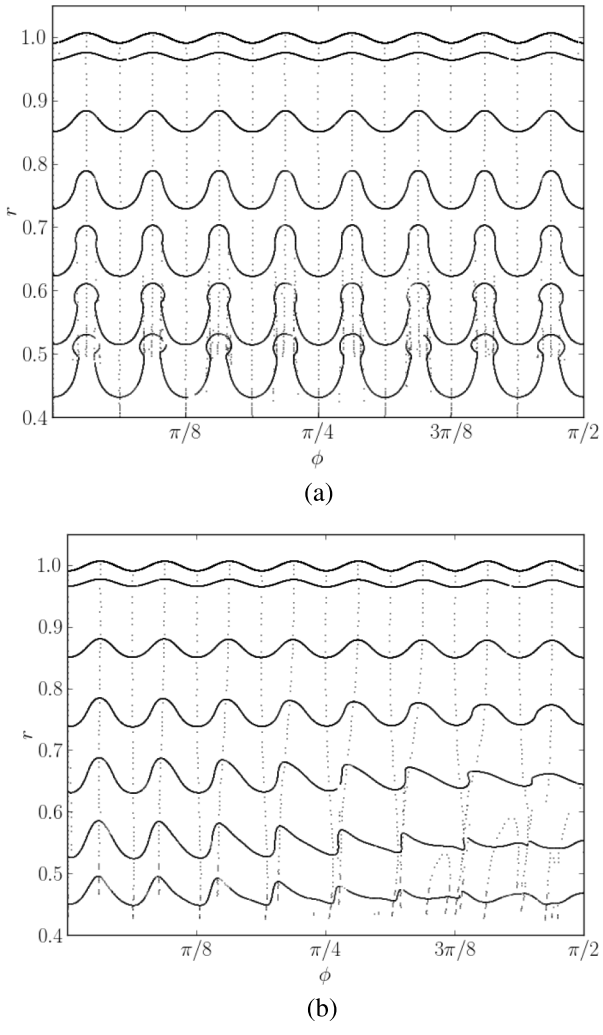

FIG. 7. Interface (DI) profile radius across ϕ-domain for cases C0-32 and C1-32-32, plotted successively at time increments $\Delta t = 0.1$. Lower interfaces are at later times. Dotted lines track the extrema of the interface over time. (a) C0. (b) C1, $\beta_{0I} = 32$.

simulation progresses, the perturbations are seen to grow rapidly up to a certain amplitude before decreasing again. This decrease is attributed to the RT instability which begins to dominate after some time. Since these problems feature a light-heavy interaction, the RT instability drives a phase inversion.

Case C1-32-32, however, shows suppression of the perturbation growth due to RM instability for moderate times. At later times, the RT instability is also suppressed. The magnetic field is seen to cause the form of the perturbation to deviate substantially from sinusoidal, and the suppression of the instability varies significantly with angular location, which is quantified next.

4. Effect of seed field strength

Figure 8 shows the perturbation amplitude η/η_0 (that is, normalized by the initial amplitude η_0) for the cases C1-4-32, C1-32-32, and C1-128-32 (that is, all tested field strengths—see Table I), for values of ϕ incremented by $\pi/8$. In each set of curves, the top curve corresponds to $0 < \phi < \pi/8$, and ϕ increases downwards. A result for C0-32 is given for comparison. The figure shows that increasing the field strength increases the maximum suppression of perturbation growth; however, increasing field strength also increases the degree of asymmetry of perturbation growth suppression. The $\beta_{0I} = 4$ (C1-4-32) result shows this especially, with perturbation amplitude profiles separating almost

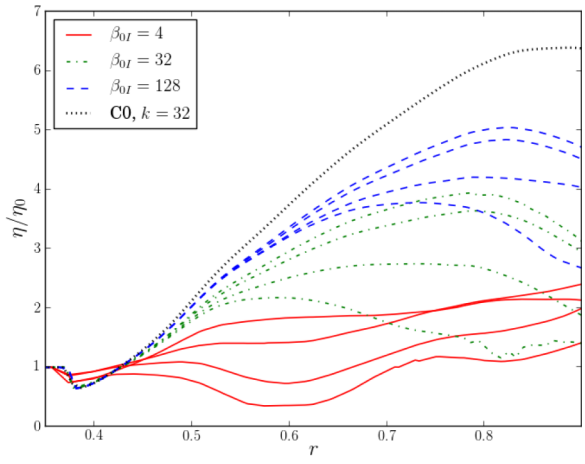

FIG. 8. Perturbation amplitude η/η_0 normalized by initial amplitude, for perturbations of the DI after IFS-DI interaction, for C1-4-32, C1-32-32, C1-128-32, and C0-32 case. Curves are plotted across ϕ, increasing from top to bottom within each set, with increments $\Delta\phi = \pi/8$.

immediately after the IFS-DI interaction (which occurs at $t \simeq 0.38$). In contrast, the $\beta_{0I} = 32, 128$ (C1-32-32 and C1-128-32) sets show roughly similar perturbation growth for early times after the interaction.

The curves for which the field is approximately normal to the DI—that is, for ϕ near zero—show the greatest amount of amplitude growth for all field strengths, while the reverse is true for ϕ near $\pi/2$, despite the observation above that vorticity-carrying waves move away from the DI where the field is normal to it, and along the DI where the field is parallel to it. This is because, following the initial flattening of the interface during the IFS-DI interaction ($t \simeq 0.38$), the vorticity near the DI around $\pi/2$ moves parallel and antiparallel to the DI in a manner which immediately counteracts perturbation growth on the DI in that region of ϕ, since the sign of the destabilizing vorticity around a given perturbation is continually changing. By contrast, the DI near $\phi = 0$ does not see oscillating sign of vorticity near a given perturbation, since the vorticity is being carried away from it. Hence, growth of perturbations in this ϕ-region is merely asymptotically decreasing. In this initial, RM-dominated phase of perturbation growth, the perturbations near $\phi = 0$ thus grow to a greater peak amplitude than that of the time-oscillating perturbations near $\phi = \pi/2$. This oscillating behaviour in time is especially clear in the lowest curve of the $\beta_{0I} = 4$ case.

For segments of the DI with high ϕ, the amplitude curve oscillates near zero suggesting a phase inversion of the DI in that region. This is due in part to the action of the vorticity in that magnetic field orientation. Furthermore, however, Figure 7(b) shows the formation of an additional critical point around $\phi = \pi/2$. This is in turn due to the sweeping action of the vorticity on the peaks near $\phi = \pi/2$ towards parts of the interface where the wavelengths remain static. The effect is that of a phase inversion in some parts of the interface, but not in others. That is, where the interface transitions from an inverted profile to a non-inverted profile, an additional peak or trough is generated.

In the medium- and weak-field cases (C1-32-32 and C1-128-32, respectively) and C0 case, there are two clear phases of perturbation growth. Initially, a RM-dominated phase occurs after the IFS-DI interaction, showing clear growth (appropriately mitigated by the presence of a field in the non-zero-field cases) of perturbations across all ϕ. At some later time, however, this growth ceases and is replaced by a decrease in amplitude, driven by a RT-dominated phase. This is shown more clearly in Figure 9, which shows amplitude growth rate $\dot{\eta}$ for $0 < \phi < \pi/8$.

In these cases, the initial RM-dominated growth persists until around $t \simeq 0.7 - 0.8$. This initial phase is comprised of two smaller subphases. First, the growth rate is positive and increasing up to a peak at $t \simeq 0.5$, before it plateaus and gradually decreases. Second, at around $t \simeq 0.75$ and beyond, the growth rate decreases more sharply, and at this point, RT-dominated phase begins. With the growth rate decreasing below zero, the perturbations begin to flatten. Figure 10 shows the density field at $t \simeq 0.8$, which corresponds roughly with the time of maximum perturbation

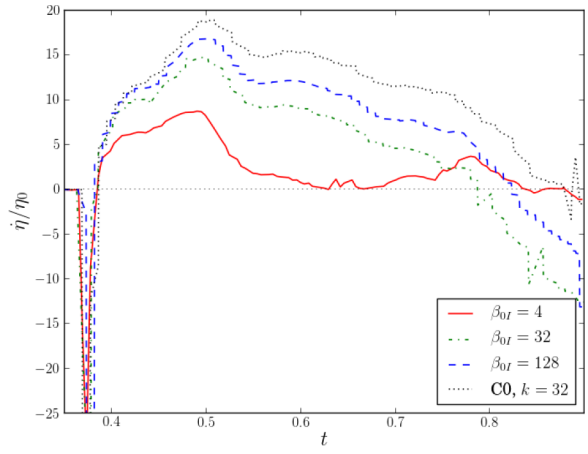

FIG. 9. Amplitude growth rate $\dot{\eta}$ for the $0 < \phi < \pi/8$ perturbation after IFS-DI interaction, for C1-4-32, C1-32-32, C1-128-32, and the C0-32 case.

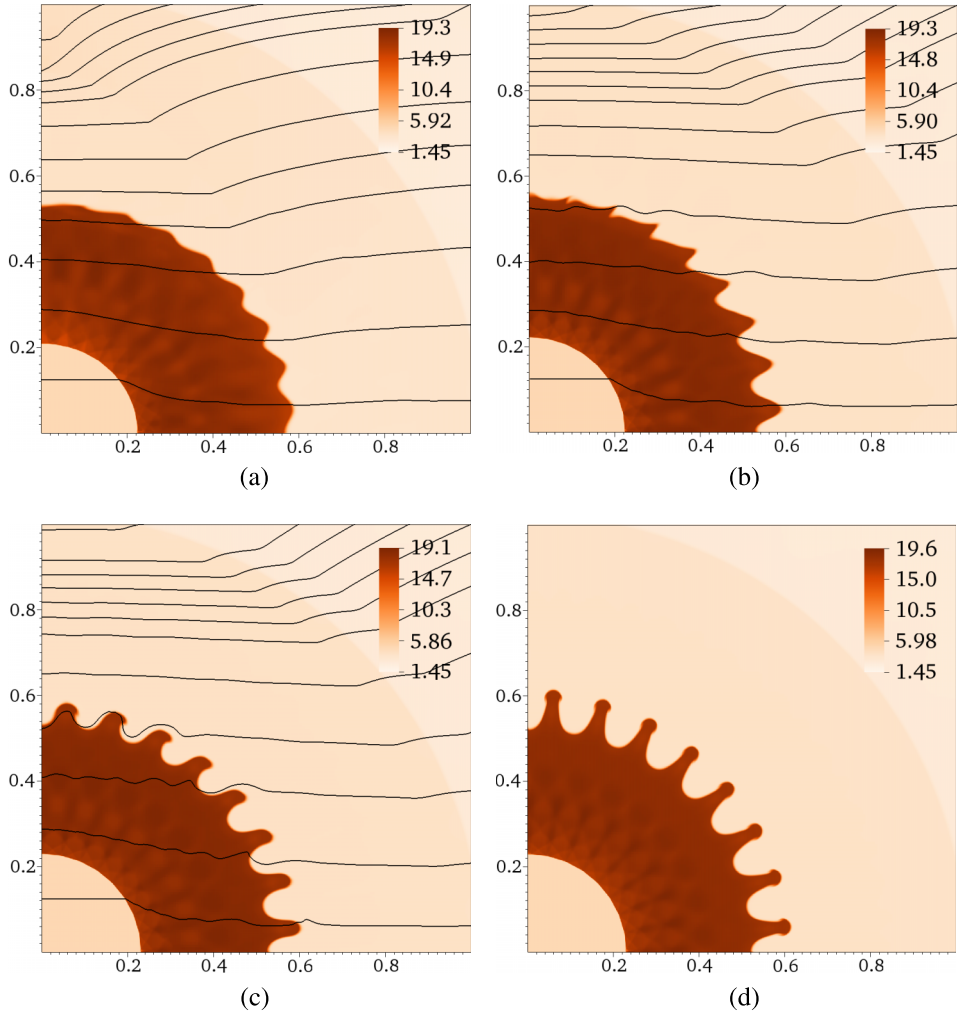

FIG. 10. Density fields showing approximately maximum perturbation amplitude at $t = 0.8$, for C1 and C0 cases. (a) C1-4-32. (b) C1-32-32. (c) C1-128-32. (d) C0-32.

growth in all cases, and immediately after the RT-driven deceleration of perturbation growth. This RT-driven decrease in amplitude occurs across all ϕ (not shown on Figure 9), suggesting that it may dominate over the RM-prompted time oscillations of the $\phi \simeq \pi/2$ perturbations. However, Figure 9 furthermore suggests that this RT-dominated growth phase, like the RM-dominated phase, is also suppressed with successively stronger seed fields; the negative gradient in $\dot{\eta}$ is ameliorated for stronger fields, approaching zero in the C1-4-32 (strong field) case.

The strong-field case C1-4-32 appears resistant to both RM- and RT-dominated growth. While it suffers a similar initial growth immediately after the IFS-DI interaction, as in the other cases, this growth plateaus quickly and, certainly for the $\phi \simeq 0$ perturbations, appears not to be affected further by RM- or RT-prompted growth.

5. Effect of perturbation wavenumber

Figure 11 shows a comparison of amplitudes and growth rates for varying initial perturbation wavenumber k, for $\beta_{0I} = 32$, and the corresponding C0 cases. The figure shows that perturbation growth is suppressed along all portions of the DI for each wavenumber. It also suggests—more clearly than Figure 8—that the initial interface growth for *any* seed field strength matches the zero-field case, and that this growth is a positive function of perturbation wavenumber. By comparison of the growth

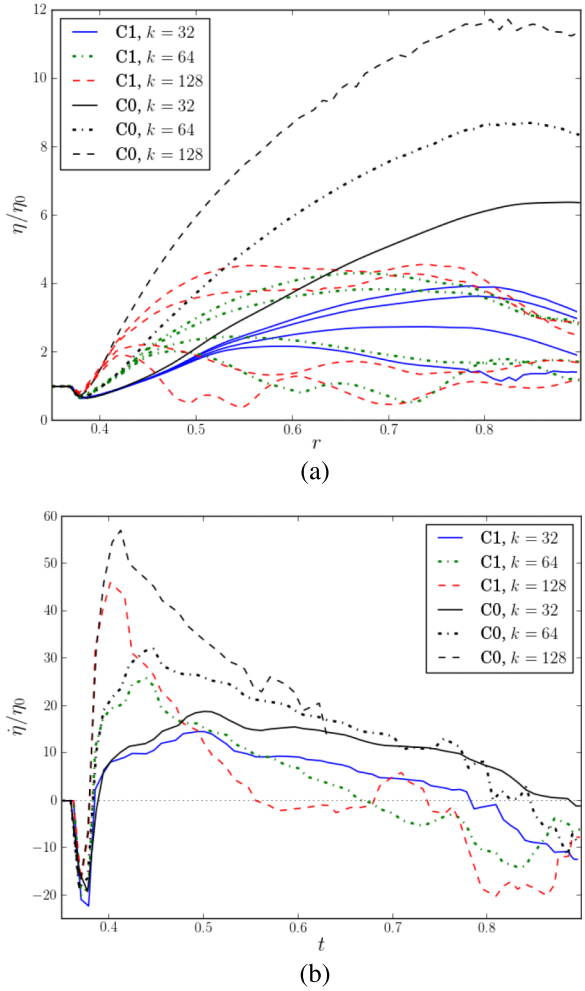

FIG. 11. Perturbation amplitude (plotted with increasing ϕ from top to bottom, with $\Delta\phi = \pi/8$) and growth rate for the $0 < \phi < \pi/8$ segment, comparing all C0 cases and C1-32-32, C1-32-64 and C1-32-128. (a) Amplitude η/η_0 (b) Growth rate $\dot{\eta}$.

rates in Figure 11(b) at $t = 0.4$, it indeed appears that the initial perturbation growth rate is roughly proportional to wavenumber, as suggested by linear RM theory.

Increasing the perturbation wavenumber also appears to increase the asymmetry in suppression. In Figure 11, the curves (each of which corresponds as usual to a segment of ϕ) separate very early, at $t = 0.4^+$, in the $k = 128$ case, while remaining compact until $t \simeq 0.5$–0.6 in the $k = 32$ case. The growth of perturbations at high ϕ (e.g., the lowest curves in each set) is also very strongly suppressed in the C1 cases, and perturbations at *all* ϕ, for $k > 32$, do not suffer a distinct, strong RT-dominated phase in the time domain considered here. The extent of perturbation growth suppression is also in general increased for greater k. For example, the C1 peak amplitudes are separated further from the C0 peak amplitudes for $k = 128$ than $k = 32$.

Based on these observations of case C1, we may summarize some key points:

1. Increasing seed field strength β_{0I} increases extent of perturbation growth suppression under both RM- and RT-dominated phases.
2. Increasing β_{0I} also increases the asymmetry of perturbation growth suppression, i.e., it increases the degree to which the growth of different wavelengths is suppressed to different extents.
3. Increasing perturbation wavenumber k increases extent of perturbation suppression and increases the initial growth rate of perturbation amplitude.
4. Increasing k generally increases nonuniformity of perturbation suppression.

6. Effect of seed field configuration

Figure 12 shows the structure of C3 cases with $k = 32$ (that is, C3-4-32, C3-32-32, C3-128-32—see Table I), across all field strengths. The time shown is relatively early, $t \simeq 0.65$, shortly after the IFS-DI interaction. The kink in the slow-shock geometry at $\phi = \pi/4$ (that is, field angle $\nu = \pi/2$) approaches the DI for the $\beta_{0I} = 4$ case (Figure 12(a)) but is not clearly visible for the weaker cases (Figures 12(b) and 12(c)). The slow shock system is known to be quite weak for low field strengths and strengthens (with a concomitant weakening of the fast shock system) as the field strength increases. Its speed also increases with the high field strength, so that it approaches the DI more quickly for lower β_{0I}.[18] The reason that the slow shock kink approaches the DI so quickly in C3-4-32 case, and not in the (corresponding) C1-4-32 case, is the high field strength at the RI in the C3 case compared to the uniform field strength in the C1 case, which itself creates a very high slow characteristic speed in that region. The interaction of the slow shock kink with the DI does complicate the flow near the DI at $\phi = \pi/4$ for the $\beta_{0I} = 4$ cases for the C3-configuration. As this interaction only occurs in a small number of cases, for conciseness we do not discuss it in detail.

The interface profile evolution for C3-32-32 (whose slow shock kink does not closely approach the DI for even late times) may be seen in Figure 13, including again for convenience the C0-32 case for comparison. As with the (equivalent) C1-32-32 case, the RM- and RT-growth phases both appear suppressed in early and late times, respectively. The observation that C3 implosion structures appear like a "doubled" form of C1 structures[18] is appropriate here; qualitatively speaking, the pattern of perturbation suppression here for $0 < \phi < \pi/4$ is very similar to the pattern in C1 for $0 < \phi < \pi/2$. In other words, features that appear over a quarter-domain in C1, here appear in an eighth-domain, with the $\pi/4$ axis acting as a symmetry plane. This is because, in the C1 case, the field-interface angle is roughly equal to the azimuth angle (i.e., $\nu \simeq \phi$), while in the C3 case, the field-interface angle is roughly double the azimuth angle ($\nu \simeq 2\phi$).

Observing now the role of choice of field configuration in extent and asymmetry of suppression of the perturbation growth, a comparison of C1-32-32 and C3-32-32 amplitude and growth rates is shown in Figure 14. In this figure, the increments for ϕ are adjusted between C1 and C3 configurations to ensure that the curve sets represent the same field angles to the DI. As the figure shows, the extent and asymmetry of suppression is very similar between the two configurations, with the C3 configuration showing a slightly increased extent of suppression over field angle.

Regarding suppression of the RM instability, there appears to be little effect in using a C3 configuration instead of a C1 configuration, since extent and asymmetry of perturbation suppression

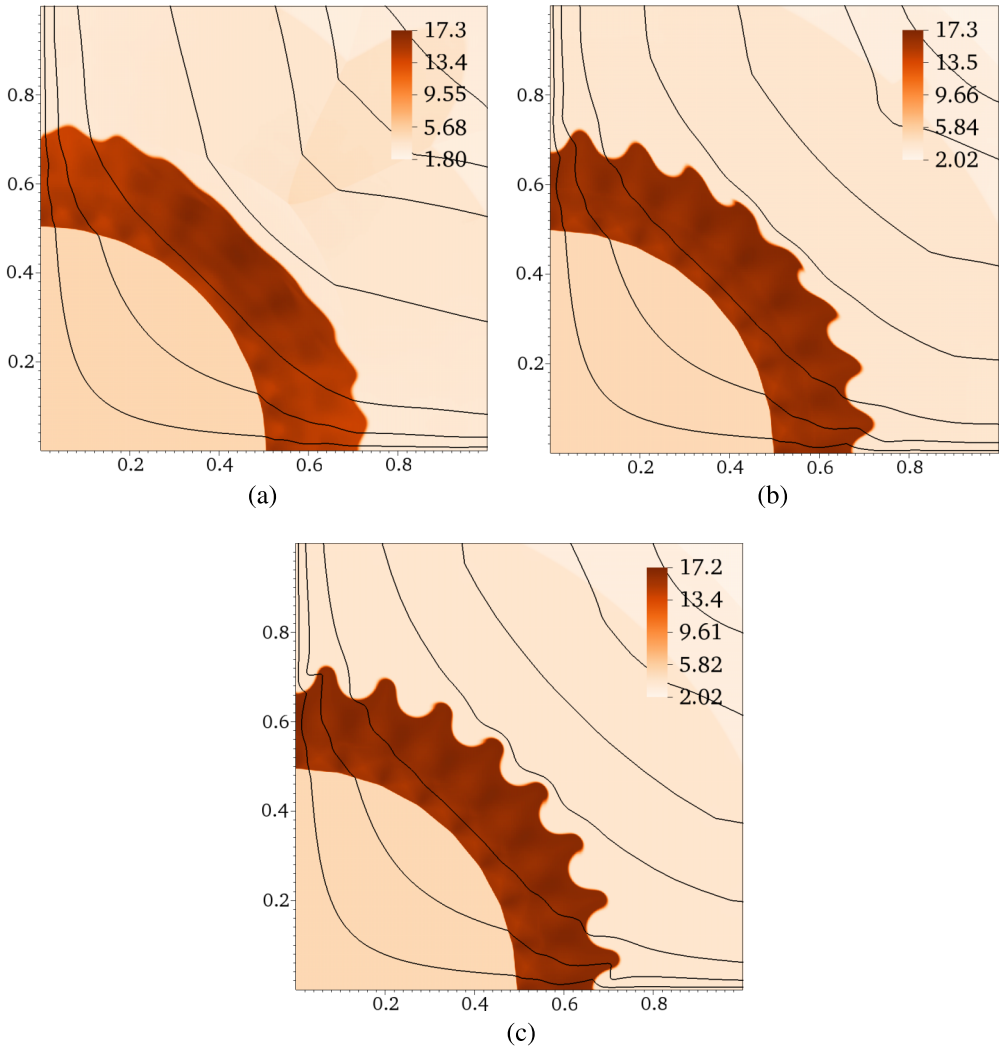

FIG. 12. Density field at $t \simeq 0.65$, for cases of C3, varying field strength. (a) C3-4-32. (b) C3-32-32. (c) C3-128-32.

are not dramatically affected by the choice. However, the degree of asymmetry in the *base* flow in a C3-configuration implosion is, for a given field strength, much reduced compared to the equivalent C1-case.[18] Comparison of these two statements suggests that, for useful suppression of the RM and RT instabilities in a collapsing flow, a saddle-like configuration would perform similarly to an equivalent uniform configuration while maintaining a much more nearly symmetric imploding base flow. In a geometric sense, it appears that increasing the number of planes of symmetry in the seed field does not appear to adversely affect instability suppression, but does in fact reduce the degree of asymmetry introduced by applying a seed field.

We finally consider the circularity of the mean DI position. Separating the interface into segments of $\Delta\phi$, each with mean position $\bar{r}_{\Delta\phi}$, we define the symmetry parameter ς, which is the standard deviation of these mean positions. Thus, an implosion with an axisymmetric DI mean position, such as C0 cases, would show $\varsigma = 0$. Figure 15 shows $1 - \varsigma$ for cases C1 and C3 and $k = 128$, under various field strengths.

As Figure 15 shows, except for the strong field $\beta_{0I} = 4$, symmetry evolution of the C1 and C3 cases are roughly comparable, with a slightly decreased degree of asymmetry (that is, deviation from circularity) in the C1 cases over their respective C3 counterparts. The strong field case deviates significantly from axisymmetry due to the ISS-DI interaction, which severely distorts the interface

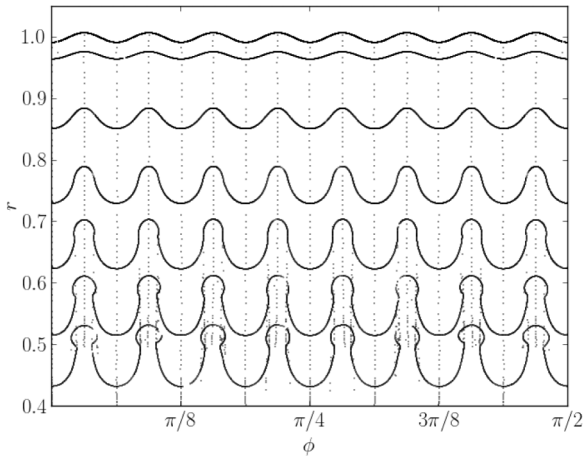

(a)

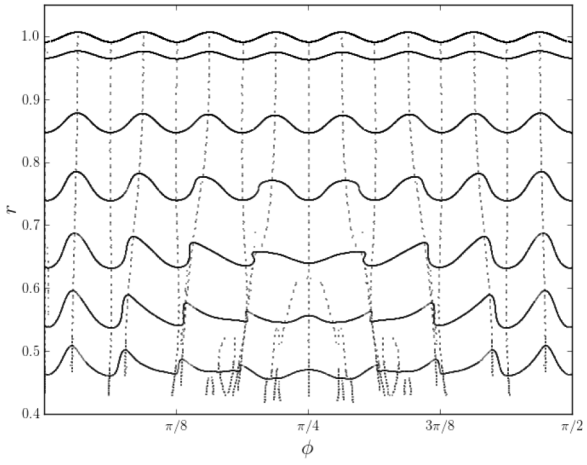

(b)

FIG. 13. Interface (DI) profile radius across ϕ-domain for cases C0-32 (identical to Figure 7(a)), C3-32-32, plotted successively at time increments $\Delta t = 0.1$. Lower interfaces are at later times. Dashed lines track extrema in the interface. (a) C0-32. (b) C3-32-32.

as a whole. This effect is greatest in the C3 strong field cases (C3-4-cases), owing to the increased strength of the ISS in that problem.

The greatest effect is provided by the field strength; ISS-DI interaction aside, the $\beta_{0I} = 32$ problems do show increased asymmetry over the $\beta_{0I} = 128$ problems, apparently to a greater degree than the choice of field configuration.

III. SPHERICAL RM INSTABILITY

The investigation into the converging RM instability in MHD is now extended into spherical geometry. The formulation and methodology for the spherical problem are distinct from the cylindrical problem and are discussed prior to presentation of results.

A. Formulation

The flow variables are non-dimensionalized as in (1), and the governing equations are ideal MHD as described in (2)-(5). Both Cartesian coordinates (x, y, z) and spherical coordinates (r, ϕ, θ) are used, with the usual transformations $x = r \sin\theta \cos\phi$, $y = r \sin\theta \sin\phi$, and $z = r \cos\theta$.

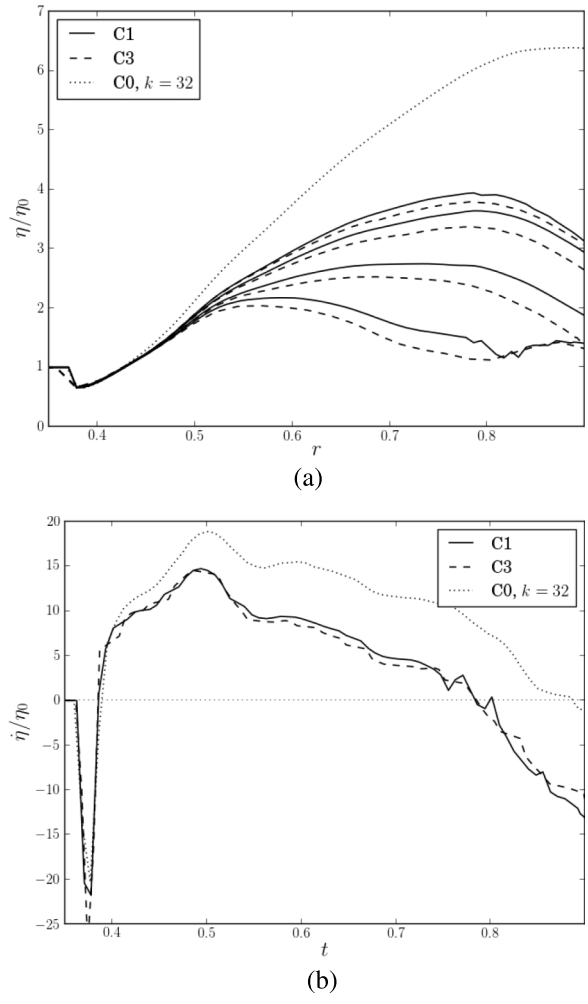

FIG. 14. Amplitude and growth rate for cases C1-32-32 and C3-32-32 configurations (see Table I for case descriptions). Curves in (a) plotted over ϕ, increasing top to bottom within each set, with an increment of $\Delta\phi = \pi/8$ for C1 and $\pi/16$ for C3. Curves in (b) plotted for $0 < \phi < \pi/8$ for C1 and $0 < \phi < \pi/16$ for C3. (a) Amplitude, η/η_0. (b) Growth rate, $\dot{\eta}$.

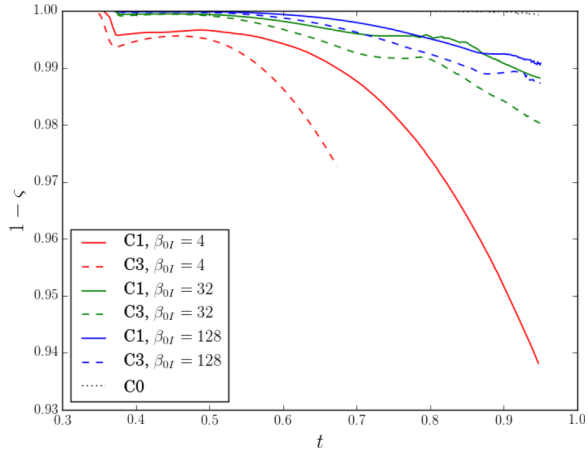

FIG. 15. Symmetry evolution of the mean DI position for cases C1 and C3 (compared to unity curve provided by C0).

The field configurations used in the spherical problem are three-dimensional analogues to those used in the cylindrical problem and are as follows:
S1: Uniform, uni-directional field

$$\mathbf{B} = B_0\hat{\mathbf{e}}_\mathbf{x}, \tag{15}$$

with the variables defined as for (8).
S3: Saddle-point field

$$\mathbf{B}(x, y, z) = B_x\hat{\mathbf{e}}_\mathbf{x} + B_r\hat{\mathbf{e}}_\mathbf{r}, \tag{16}$$

where the subscript r indicates a radial component in the $y-z$ plane and $\hat{\mathbf{e}}_\mathbf{r}$ is the associated unit vector. This field may be generated by two current loops of opposite direction in $y-z$ planes centred on the x-axis at $x_i = \{7, -7\}$.[18] The field components may be found according to the work of Smythe,[30]

$$B_x = \sum_{i=1}^{2} \alpha_i B_0 \frac{1}{\pi\sqrt{Q_i}}\left[E(k_i)\frac{1-\varrho^2-\chi_i^2}{Q-4\varrho} + K(k_i)\right], \tag{17}$$

$$B_r = \sum_{i=1}^{2} \alpha_i B_0 \frac{\xi_i}{\pi\sqrt{Q_i}}\left[E(k_i)\frac{1+\varrho^2+\chi_i^2}{Q-4\varrho} - K(k_i)\right], \tag{18}$$

where $a = 7$ sets the radius of the current loops, approximately consistent with that of Chang *et al.*,[13] $Q_i = (1+\varrho)^2 + \chi_i^2$, $k_i = \sqrt{\frac{4\varrho}{Q_i}}$, $\varrho = r_{yz}/a$, $\chi_i = (x - x_i)/a$, $\xi_i = (x - x_i)/r_{yz}$, and r_{yz} is the radial position in the $y-z$ plane. K and E are elliptic integrals of the first and second kinds, respectively. In this configuration, the field strength at the origin of the domain is zero.

The density interface is initialized similarly to (11), with $\mathcal{A} = 2/3$,

$$\rho(r, \phi, \theta) = \frac{1}{2}\left(1 - \frac{|\mathcal{A}|}{\mathcal{A}}\tanh\left[\mu(r - \zeta_0(\phi, \theta))\right]\right). \tag{19}$$

For this geometry, we desire a perturbation with more than a single wavenumber in ϕ, seeking a more isotropic perturbation. We follow the work of Lombardini *et al.*[24] in their creation of a distribution of wavenumbers centred at a dominant wavenumber, with an expansion of $\zeta_0(\theta, \phi)$ using the real spherical harmonics basis,

$$\zeta_0(\theta, \phi) = r_0 - \eta_0 \sum_{l=0}^{\infty}\sum_{m=-l}^{l} f_{lm}Y_{lm}(\theta, \phi), \tag{20}$$

where $Y_{lm}(\theta, \phi)$ is a real spherical harmonic of order l, m, and

$$f_{lm} = \sqrt{(2l+1)P_l}\frac{\cos(2\pi\omega_l^m)}{\sqrt{\sum_{j=-l}^{l}\cos(2\pi\omega_l^j)^2}}, \tag{21}$$

with ω_l^m and ω_l^j as randomly generated numbers in $(0, 1)$. The constant P_l sets a power spectrum, maintaining a Gaussian perturbation mode distribution around a dominant approximate wavenumber k and is defined as

$$P_l = \frac{1}{4(2k+1)}\frac{1}{\sigma_0\sqrt{2\pi}}\exp\left(-\frac{(l-k)^2}{2\sigma_0^2}\right), \tag{22}$$

where σ_0 is the standard deviation of the distribution, set here to $\sigma_0 = k/30$, following the work of Lombardini *et al*. The coefficients and power spectrum are derived by investigation[31] of Lombardini *et al*. This method is advantageous for its statistical isotropy and avoidance of singularities in geometry.[24] Using this method for the spherical DI has the further advantage of representing a real perturbation field somewhat more realistically; Lombardini *et al.*[24] note that it represents a single dominant perturbation wavenumber, as opposed to a truly multimodal distribution. We however maintain a single-mode (or single-dominant-mode) distribution in this study for additional clarity in

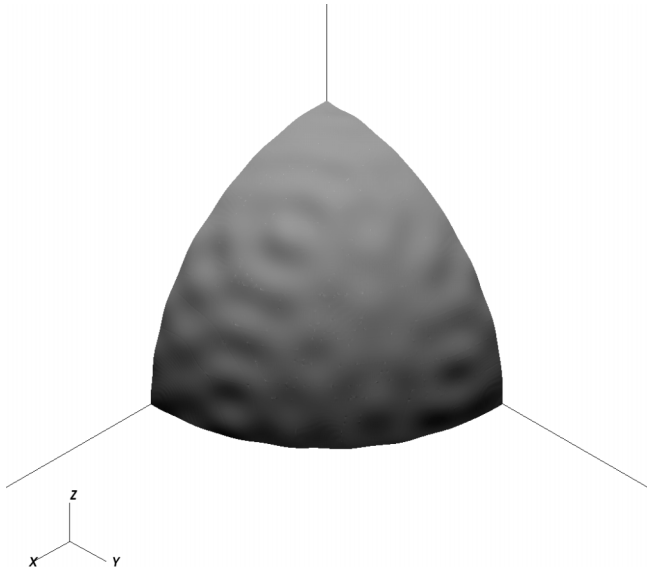

FIG. 16. The perturbed DI in spherical geometry.

the shock refraction and perturbation growth behaviours. The characteristic amplitude parameter is set to $\eta_0 = \pi/(5k) = \pi/160$; this provides a perturbation surface similar to the cylindrical geometry $k = 32$ case. Figure 16 shows the resultant perturbed DI in spherical geometry with angled lighting to highlight the perturbations.

The driving shocks are initialized using Riemann problems and identically to the cylindrical problem, using (13) and (14). (Due to the higher dimensionality of the problem, the Mach number of the shock when it reaches the DI is now approximately 2.5 in the hydrodynamic case.) The initial condition is then completely specified and can be seen in principal Cartesian planes in Figure 17.

The spherical cases are designated according to field configuration and perturbation wavenumber, as in the cylindrical problem. The abbreviations for each case can be found in Table II. In this analysis, only a dominant perturbation wavenumber $k = 32$ is considered.

B. Methodology

In these simulations, the interface regularization parameter μ was set to $\mu = 270$ for an initial interface width of approximately 6-7 cells along the Cartesian axes.

1. Numerical convergence

The grid convergence of the perturbed three-dimensional simulations is tested by running unrefined resolutions of 36^3, 48^3, and 64^3, which have associated effective resolutions (also on three levels of adaptive refinement) of 288^3, 376^3, and 512^3. We find the perturbation amplitude of the DI by subtracting the DI profile for a given perturbed simulation from the same for the corresponding unperturbed simulation; the highest-amplitude perturbation in the $x - y$ plane may then be plotted over time, and the numerical integral calculated as in the cylindrical case converges with order 1.19 with an associated Richardson-extrapolated error on the finest mesh of 1.5%.

At any given time, *monotonic* convergence of the DI profile itself is difficult to verify consistently, especially at the boundaries of the computational domain. However, the l1-norm of the linearly interpolated profile in the $x - y$ plane, for example, differs between the second-finest and finest meshes by approximately 3.4% at $t = 0.65$, which is a well-advanced time in the three-dimensional simulations.

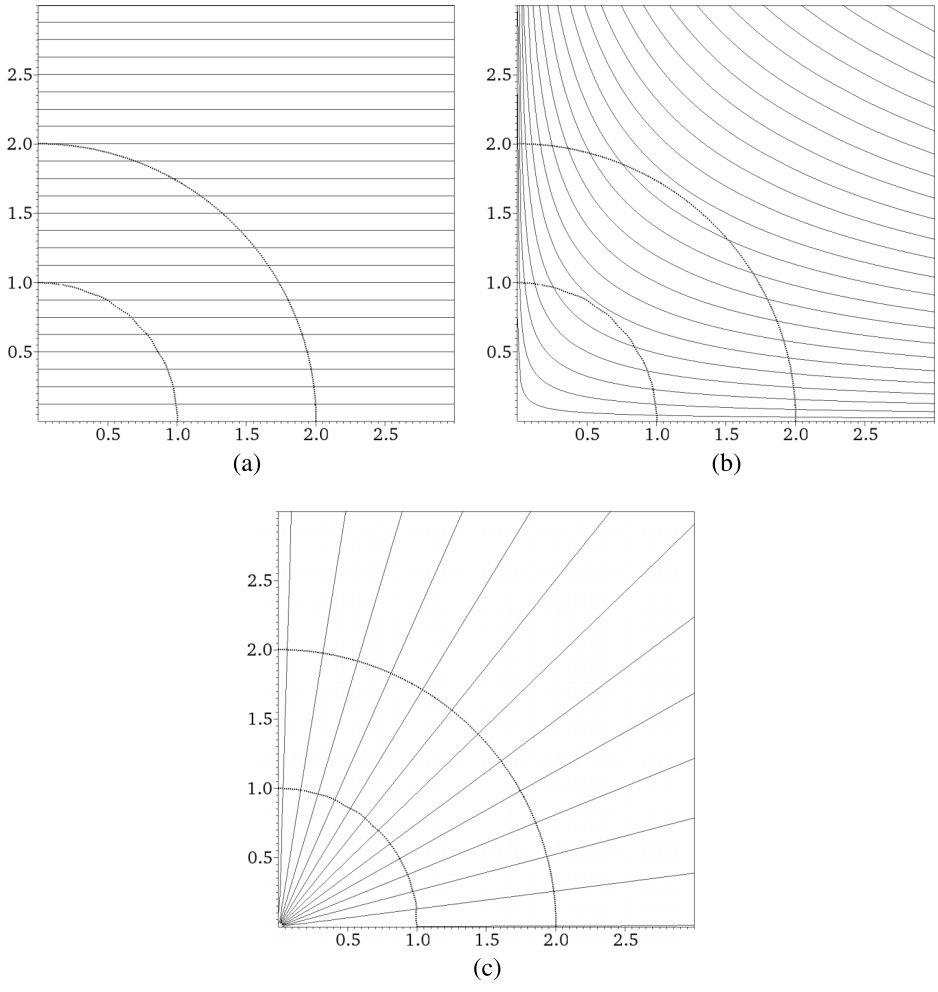

FIG. 17. Initial condition density fields with overlaid magnetic field lines for all cases. Shown with dominant spherical perturbation wavenumber $k = 32$. (a) Case S1, $x - y$ plane. (b) Case S3, $x - y$ plane. (c) Case S3, $y - z$ plane.

While the resolution here appears significantly lower than that of the cylindrical simulations, the perturbation wavenumber being investigated in 3D (32) is lower than that which the 2D simulations were designed to resolve (128). Thus, the minimum resolution per wavelength is a factor of ≈2 lower in the 3D case, which leads to greater departures from the exact solution. This is somewhat mitigated, however, by the greater growth in the 3D case (presented in the next section) causing the

TABLE II. Description of case abbreviations for spherical geometry, indicating field configuration, strength, and dominant wavenumber. These cases are run at unrefined mesh resolutions of 64^3 with three levels of refinement for effective resolutions of 512^3. S0-cases have no seed field, S1-cases have uniform unidirectional seed fields, and S3-cases have saddle-point seed field.

Case abbreviation	Field strength, β_{0I}	Dominant wavenumber, k
S0-32	∞ (none)	32
S1-4-32	4	32
S1-128-32	128	32
S3-4-32	4	32
S3-128-32	128	32

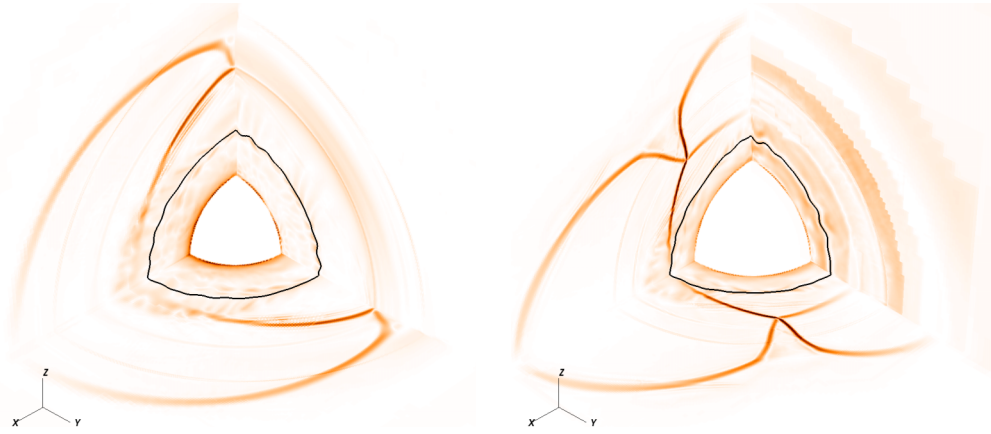

FIG. 18. Developed absolute vorticity field along principal planes for strong-field spherical cases at comparable time. DI shown by black line. Colour scale adjusted to show primary flow features. See Table II for description of case abbreviations. (a) S1-4-32, $t = 0.63$. (b) S3-4-32, $t = 0.56$.

perturbations to be more highly resolved at late times. This may explain why the error estimate for the 3D case is only slightly greater than that for the 2D case despite having half the resolution per wavelength.

C. Results

1. Wave structure

The S-cases constitute the three-dimensional problems in this study. Figure 18 shows combined slices for the three principal planes on the octant interior faces, showing vorticity magnitude, and a solid line for the DI location after IFS-DI interaction, for cases S1-4-32, S3-4-32 (see Table II). Clearly visible from the inside outwards are the transmitted fast shock TF, the DI (highlighted), the ISS, and the outward-moving slow expansion. In Figure 18(a), the $y - z$ plane is normal to

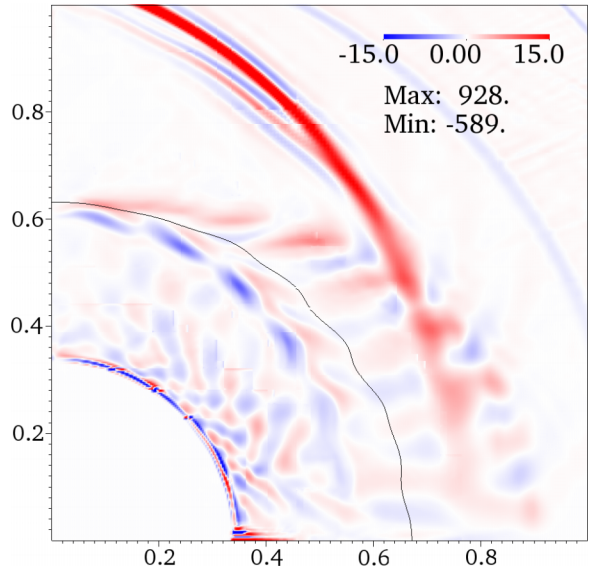

FIG. 19. z-vorticity around the DI (shown by black line) at $t = 0.63$, for S1-4-32. Colour scaled to highlight the main flow features.

the field lines and so shows a much sparser structure, as expected from the associated Riemann problem.[18] Due to the higher dimensionality of the problem, the imploding waves—in particular the TF wave—converge to the domain centre much more quickly than in the cylindrical case.

2. Effect of local seed field orientation

In both S1 and S3, the $x-y$ and $x-z$ planes remain analogous to the corresponding C-cases. The wave structure in the $x-y$ plane of S1-4-32 is shown in Figure 19, showing the expected configuration of transmitted and reflected slow and fast waves. The effect of the ISS on the DI geometry is however amplified, as will be discussed in Sec. III C 3. (In Figure 19, some additional vorticity is visible near the TF wave on the x-axis. This is a numerical effect brought about by the

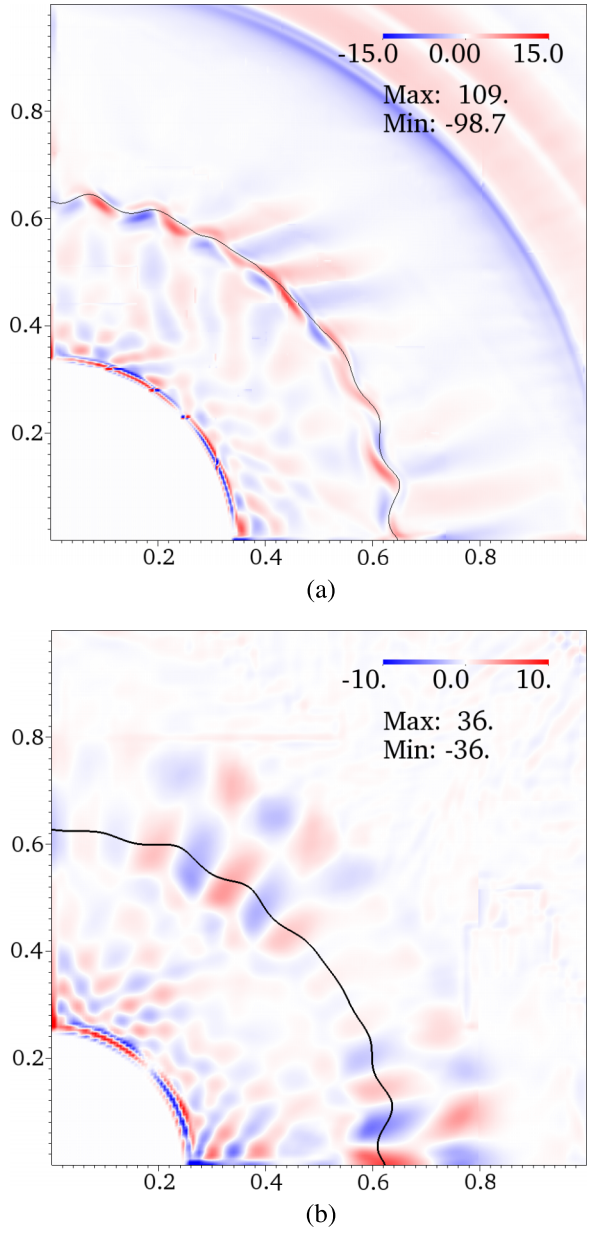

FIG. 20. x-vorticity (coloured) and DI (black line) in the $y-z$ plane for S1-4-32 and S3-4-32. (a) $S1, t = 0.66$. (b) $S3, t = 0.67$.

boundary conditions, appears only the boundary, and is avoided in any statistics regarding the DI throughout this study.)

Careful examination of Figure 18 for both cases suggests that the perturbation growth is suppressed differently in the $y-z$ plane than in others. This is not surprising given that the $y-z$ plane sees a different field configuration than the other planes: in S1, the field is everywhere normal to the plane and tangential to the DI, and in S3, it is everywhere normal to the DI.

The resulting vorticity transport in this plane is shown in Figure 20. Now in S1 (20(a)), the RM- and RT-generated vorticity remains in the vicinity of the DI, since the slow reflected and transmitted waves now travel into and out of the plane. In S3 (20(b)), the vorticity is carried away normally from the DI. This latter case additionally provides a convincing example of both the continuous development of RT-vorticity later in the implosion and its continuous advection away from the DI along magnetic field lines.

3. Extent of asymmetry of perturbation growth suppression

The extent of the suppression of the perturbation growth in each plane will now be considered. Rather than examining an explicit time-evolution in a given plane as in the C-cases, we seek to identify perturbation amplitude in all principal planes at a given time in order to provide a complete picture of each case. Such a representation for S1-4-32 may be seen in Figure 21: for a given case, the top-right, top-left, and bottom-left quadrants represents the $x-y$, $y-z$, and $x-z$ planes, respectively, while the bottom-right quadrant shows the HD case (S0-32) at the simulation time. The plots are density contours, with the DI highlighted and coloured according to local amplitude. Figure 22 shows the same configuration for $\beta_{0I}=128$. Since the perturbations on the DI are not uniform in the spherical geometries, the local perturbation amplitude is estimated here by subtracting the interface location of the perturbed simulation from that of the unperturbed simulation.

In the S1-4-32 (and S3-4-32) cases, the symmetry of the DI as a whole is disturbed, and towards $\phi=\pi/2$ sees a great variation of the gross interface position with ϕ with almost zero amplitude of perturbation. The distortion of the DI in this case is due largely to the ISS-DI interaction. The distortion in S3-4-32 is particularly severe and similarly to the cylindrical geometries, we do not consider this case at length. The perturbation growth is greatly suppressed, showing a maximum amplitude of 43% of the HD (S0) equivalent at time $t=0.64$. The maximum amplitude in the S1 case occurs in the $y-z$ plane, where the magnetic field lines are everywhere tangent to the DI.

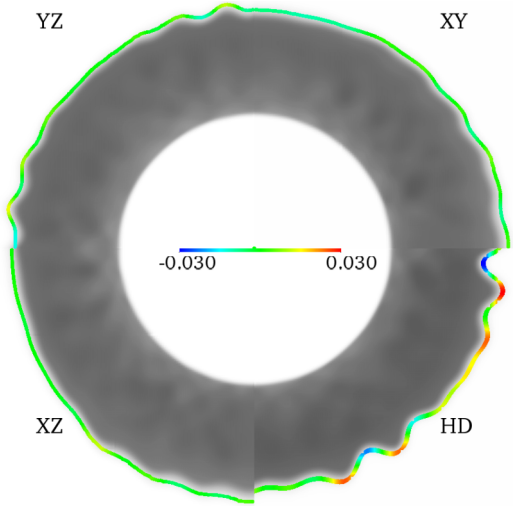

FIG. 21. Density field contour on principal planes for S1-4-32 with the interface (DI) highlighted in colour. Top right, top left, and bottom left quadrants are $x-y$, $y-z$, and $x-z$ planes of the S1 case, respectively; bottom right quadrant is the $y-z$ plane of the S0-32 case (see Table II). Interface highlights are coloured according to amplitude from the unperturbed interfaces. S1-4-32 case at $t=0.64$, S0-32 at $t=0.63$.

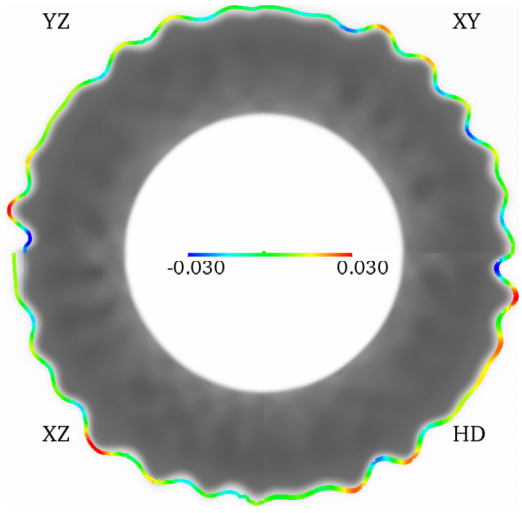

FIG. 22. Quadrant-diagram for S1-128-32 with configuration as outlined in Figure 21. S0-32 case shown at $t = 0.63$, S1-128-32 at $t = 0.64$.

This is an example of how a seed magnetic field added with the purpose of minimizing asymmetry of the collapsing flow, if applied injudiciously, may successfully suppress a certain hydrodynamic instability but introduce a secondary adverse effect. On the other hand, the $\beta_{0I} = 128$ (S1-128-32) cases retain a low degree of gross DI asymmetry but also sees sizeable perturbation growth of 95% of the HD equivalent at $t = 0.64$ in the $y - z$ plane.

Figure 23 shows the perturbation growth in the principal planes of the S3-128-32 case. By comparison with Figure 22, the extent of suppression is similar, showing a maximum amplitude of 97% in the $y - z$. The field strength $\beta_{0I} = 128$ is therefore ineffective in suppressing the maximum perturbation amplitude growth of the RM instability in the S-cases. The root-mean-square (RMS) perturbation amplitudes across the entire interface, however, are reduced to 28% (S1-4-32), 80% (S1-128-32), and 87% (S3-128-32) of the S0-32 cases, at $t \simeq 0.64$.

Figure 24 shows the time-evolution of the root-mean-square perturbation amplitude across the whole interface in the non-zero field cases compared to the largest-amplitude perturbation in the

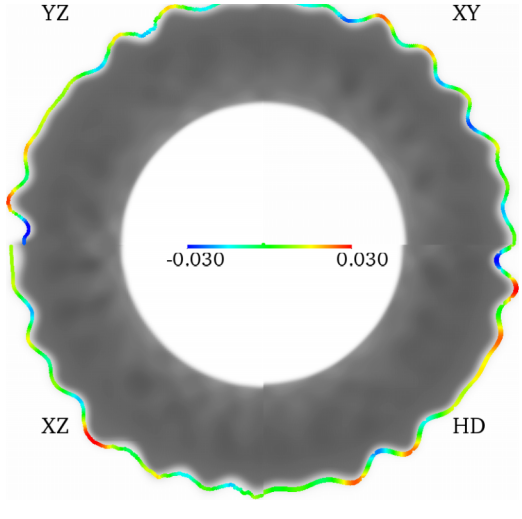

FIG. 23. Quadrant-diagram for S3-128-32 with configuration as outlined in Figure 21. S0-32 at $t = 0.63$, S3-128-32 at $t = 0.67$.

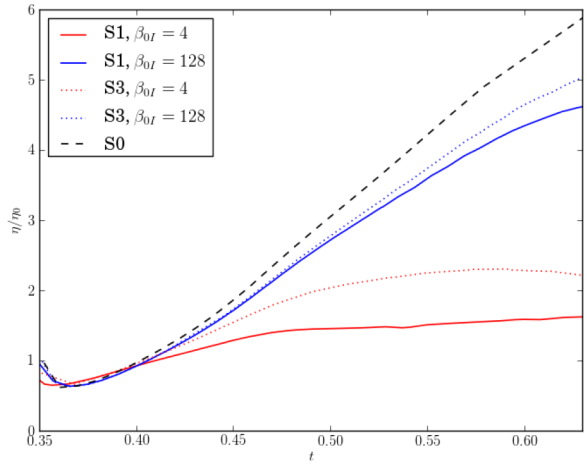

FIG. 24. Growth of the root-mean-square amplitude perturbation in cases S1 and S3 across the whole interface, compared with the S0 case.

S0 (HD) case. The perturbation amplitudes in this figure were determined by measuring the interface maximum and minimum in the angular segment of size $\pi/8$ which contains the perturbation in question. At all times shown, the perturbation growth remains suppressed in the S1 and S3 cases over the S0 case. As in the C-cases, seed field strength has a greater effect on the perturbation growth than does the choice of configuration. However, comparing Figures 24 and 8, for a given field strength, the three-dimensional RM instability (S-case) appears less suppressed than the corresponding two-dimensional instability (C-case).

The suppressive capacity of the RM instability of the field configurations S1 and S3 does not appear dramatically different for the given strength, particularly for $\beta_{0I} = 128$. This is in line with the conclusion for the cylindrical cases C1 and C3. For $\beta_{0I} = 4$, however, the S3 case appears significantly less suppressed than in S1. This is likely due to the ISS-DI interaction, which has an obvious distortive effect on the spherisymmetry of the interface as a whole, under *strong* seed fields. This effect is, however, distinct from the large-scale effect of the seed field of the dynamics of the implosion as a whole, which Mostert *et al*. considered.[18]

For $\beta_{0I} = 128$, we also find that the DI is similarly asymmetrical for the S1 and S3 cases. The DI mean position and perturbation suppression asymmetry are then comparable for the S1 and S3 cases. The distinguishing factor in the choice between the two configurations is supplied by the asymmetry in the *primary imploding shocks*, as studied previously: C3 and S3 type implosions see a lower degree of asymmetry in all planes in the primary compressive shocks (which in all studied cases in Mostert *et al*. were the IFS) than the respective C1 and S1 configurations.[18] This suggests that these saddle-point fields on the whole retain flows closer to true axi- or spherisymmetry than their uniform counterparts and opens the door for study into configurations with perhaps more planes of symmetry than even the S3 type seen here.

IV. CONCLUSION

We examined the effect of two plausible magnetic field configurations in cylindrical and spherical converging flow problems on the growth rate of the RM instability and to a lesser extent the RT instability, in the framework of ideal magnetohydrodynamics. The configurations included a uniform, unidirectional field and a field with a saddle-point at the centre of the domain. We varied field strength and the perturbation wavenumber on the density interface.

All cases with an applied seed field showed suppression of the RM and RT instabilities. The extent of suppression increased with seed field strength but was insensitive to the field configuration. The mechanism of suppression was determined to be transport of baroclinically generated vorticity away from or along the interface, depending on the local orientation of magnetic

field to the interface. This anisotropic suppression mechanism also affected the extent to which perturbations on different portions of the interface were suppressed. This non-uniformity became more pronounced and manifested sooner after the shock-interface interaction with increasing field strength. Growth of perturbations where the field was oriented nearly parallel to the interface was suppressed to a greater extent than those with a large normal field component. The RM and RT instabilities were also suppressed in three dimensions. However, the extent of suppression was generally smaller, particularly for low field strengths, compared to the cylindrical cases, and the difference in extent of suppression with field-interface angle was not as well distinguished for low field strengths.

The saddle-point configuration (that is, the C3 and S3 cases) did not provide significantly different extent or asymmetry of perturbation growth suppression compared to the uniform-field configuration. Typically, however, a saddle-point configuration exhibits a lower degree of distortion in the imploding flow relative to the uniform, unidirectional configuration.[18] This suggests that, in a paradigm of minimizing distortion in an imploding flow with respect to both hydrodynamic instability (i.e., the RM, RT instabilities in this case) and the base flow, a saddle-configuration may be better suited.

Further research may be conducted into this area. For example, one may also consider the effect of Atwood number, the effect of varying initial pressure or density ratio across the Riemann interface, which is equivalent to varying incident shock Mach number, seed field configurations different again from what we have studied so far, and heavy-to-light shock-interface interactions or multi-interface systems.

ACKNOWLEDGMENTS

This research was partially supported under Australian Research Council's Discovery Projects funding scheme (Project No. DP120102378). W. Mostert is supported by an Australian Post-graduate Award. Dr Wheatley is the recipient of an Australian Research Council Discovery Early Career Researcher Award (Project No. DE120102942). This work was partially supported by the KAUST Office of Sponsored Research under Award URF/1/2162-01.

[1] J. D. Lindl, P. Amendt, R. L. Berger, S. G. Glendinning, S. H. Glenzer, S. W. Haan, R. L. Kauffman, O. L. Landen, and L. J. Suter, "The physics basis for ignition using indirect-drive targets on the National Ignition Facility," Phys. Plasmas **11**, 339–491 (2004).
[2] R. D. Richtmyer, "Taylor instability in shock acceleration of compressible fluids," Commun. Pure Appl. Math. **13**, 297–319 (1960).
[3] E. Meshkov, "Instability of the interface of two gases accelerated by a shock wave," Fluid Dyn. **4**, 101 (1969).
[4] L. Rayleigh, *Scientific Papers* (Dover, New York, 1965), Vol. 2.
[5] G. Taylor, "The instability of liquid surfaces when accelerated in a direction perpendicular to their planes, I," Proc. R. Soc. London, Ser. A: Math. Phys. Sci. **201**, 192 (1950).
[6] R. Samtaney, "Suppression of the Richtmyer-Meshkov instability in the presence of a magnetic field," Phys. Fluids **15**, L53–L56 (2003).
[7] V. Wheatley, R. Samtaney, and D. I. Pullin, "The Richtmyer-Meshkov instability in magnetohydrodynamics," Phys. Fluids **21**, 082102 (2009).
[8] V. Wheatley, D. I. Pullin, and R. Samtaney, "Regular shock refraction at an oblique planar density interface in magnetohydrodynamics," J. Fluid Mech. **522**, 179–214 (2005).
[9] V. Wheatley, D. I. Pullin, and R. Samtaney, "Stability of an impulsively accelerated density interface in magnetohydrodynamics," Phys. Rev. Lett. **95**, 125002 (2005).
[10] V. Wheatley, R. Samtaney, D. I. Pullin, and R. M. Gehre, "The transverse field Richtmyer-Meshkov instability in magnetohydrodynamics," Phys. Fluids **26**, 016102 (2014).
[11] V. Wheatley, R. Gehre, R. Samtaney, and D. I. Pullin, "The magnetohydrodynamic Richtmyer-Meshkov instability: The oblique field case," in *29th International Symposium on Shock Waves* (Springer, New York, 2013).
[12] T. Sano, T. Inoue, and K. Nishihara, "Critical magnetic field strength for suppression of the Richtmyer-Meshkov instability in plasmas," Phys. Rev. Lett. **111**, 205001 (2013).
[13] P. Y. Chang, G. Fiksel, M. Hohenberger, J. P. Knauer, R. Betti, F. J. Marshall, D. D. Meyerhofer, F. H. Séguin, and R. D. Petrasso, "Fusion yield enhancement in magnetized laser-driven implosions," Phys. Rev. Lett. **107**, 035006 (2011).
[14] M. Hohenberger, P.-Y. Chang, G. Fiksel, J. P. Knauer, R. Betti, F. J. Marshall, D. D. Meyerhofer, F. H. Séguin, and R. D. Petrasso, "Inertial confinement fusion implosions with imposed magnetic field compression using the OMEGA laser," Phys. Plasmas **19**, 056306 (2012).
[15] L. J. Perkins, B. G. Logan, G. B. Zimmerman, and C. J. Werner, "Two-dimensional simulations of thermonuclear burn in ignition-scale inertial confinement fusion targets under compressed axial magnetic fields," Phys. Plasmas (1994-present) **20**, 072708 (2013).

[16] A. B. Sefkow, S. A. Slutz, J. M. Koning, M. M. Marinak, K. J. Peterson, D. B. Sinars, and R. A. Vesey, "Design of magnetized liner inertial fusion experiments using the Z facility," Phys. Plasmas (1994-present) **21**, 072711 (2014).
[17] M. G. Haines, "A review of the dense Z-pinch," Plasma Phys. Controlled Fusion **53**, 093001 (2011).
[18] W. Mostert, V. Wheatley, R. Samtaney, and D. I. Pullin, "Effects of seed magnetic fields on magnetohydrodynamic implosion structure and dynamics," Phys. Fluids (1994-present) **26**, 126102 (2014).
[19] D. I. Pullin, W. Mostert, V. Wheatley, and R. Samtaney, "Converging cylindrical shocks in ideal magnetohydrodynamics," Phys. Fluids (1994-present) **26**, 097103 (2014).
[20] G. Whitham, "On the propagation of shock waves through regions of non-uniform area or flow," J. Fluid Mech. **4**, 337–360 (1958).
[21] R. F. Chisnell, "The normal motion of a shock wave through a non-uniform one-dimensional medium," Proc. R. Soc. London, Ser. A: Math. Phys. Sci. **232**, 350–370 (1955).
[22] B. Srinivasan and X.-Z. Tang, "The mitigating effect of magnetic fields on Rayleigh-Taylor unstable inertial confinement fusion plasmas," Phys. Plasmas (1994-present) **20**, 056307 (2013).
[23] Q. Zhang and M. J. Graham, "A numerical study of Richtmyer-Meshkov instability driven by cylindrical shocks," Phys. Fluids **10**, 974–992 (1998).
[24] M. Lombardini, D. Pullin, and D. Meiron, "Turbulent mixing driven by spherical implosions. Part 1. Flow description and mixing-layer growth," J. Fluid Mech. **748**, 85–112 (2014).
[25] M. Lombardini and D. I. Pullin, "Small-amplitude perturbations in the three-dimensional cylindrical Richtmyer-Meshkov instability," Phys. Fluids **21**, 114103 (2009).
[26] J. Goedbloed, R. Keppens, and S. Poedts, *Advanced Magnetohydrodynamics* (Cambridge University Press, 2010).
[27] R. Samtaney, P. Colella, T. J. Ligocki, D. F. Martin, and S. C. Jardin, "An adaptive mesh semi-implicit conservative unsplit method for resistive MHD," J. Phys.: Conf. Ser. **16**, 40 (2005).
[28] P. Colella, D. Graves, J. Johnson, H. Johansen, N. Keen, T. Ligocki, D. Martin, P. McCorquodale, D. Modiano, P. Schwartz, T. Sternberg, and B. Van Straalen, Chombo Software Package for AMR Applications Design Document, Lawrence Berkeley National Laboratory, Applied Numerical Algorithms Group, 2012.
[29] F. Stern, R. V. Wilson, H. W. Coleman, and E. G. Paterson, "Comprehensive approach to verification and validation of CFD simulations—Part 1: Methodology and procedures," J. Fluids Eng. **123**, 793 (2001).
[30] W. Smythe, *Static and Dynamic Electricity* (McGraw-Hill Book Company, 1950).
[31] M. Lombardini, D. Pullin, and D. Meiron, "Turbulent mixing driven by spherical implosions. Part 2. Turbulence statistics," J. Fluid Mech. **748**, 113–142 (2014).